

Microenvironment reconstitution of highly active Ni single atoms on oxygen-incorporated Mo₂C for water splitting

Received: 15 June 2023

Accepted: 25 January 2024

Published online: 13 February 2024

Check for updates

Mengyun Hou^{1,4}, Lirong Zheng^{2,4}, Di Zhao¹✉, Xin Tan³, Wuyi Feng¹, Jiantao Fu¹, Tianxin Wei¹, Minhua Cao¹✉, Jiatao Zhang¹✉ & Chen Chen³✉

The rational design of efficient bifunctional single-atom electrocatalysts for industrial water splitting and the comprehensive understanding of its complex catalytic mechanisms remain challenging. Here, we report a Ni single atoms supported on oxygen-incorporated Mo₂C via Ni-O-Mo bridge bonds, that gives high oxygen evolution reaction (OER) and hydrogen evolution reaction (HER) bifunctional activity. By *ex situ* synchrotron X-ray absorption spectroscopy and electron microscopy, we found that after HER, the coordination number and bond lengths of Ni-O and Ni-Mo (Ni-O-Mo) were all altered, yet the Ni species still remain atomically dispersed. In contrast, after OER, the atomically dispersed Ni were agglomerated into very small clusters with new Ni-Ni (Ni-O-Ni) bonds appeared. Combining experimental results and DFT calculations, we infer the oxidation degree of Mo₂C and the configuration of single-atom Ni are both vital for HER or OER. This study provides both a feasible strategy and model to rational design highly efficient electrocatalysts for water electrolysis.

Electrochemical water splitting is widely regarded as one of the most important and promising pathways to convert renewable energy into high-purity hydrogen and oxygen^{1–4}. For a continuous overall water splitting process in practical, pairing the two electrode reactions together in an integrated electrolyser is difficult because of the mismatch of pH ranges in which these catalysts are stable and remain the most active^{5–8}. In addition, producing different catalysts for both monofunctional catalysts requires different equipment and processes, which could increase the cost compared to bifunctional catalysts. Therefore, compared to monofunctional catalysts, bifunctional catalysts are relatively favorable options for overall water decomposition⁹. Currently, Pt-based materials and Ir/Ru-based materials are the benchmark in HER and OER catalysts, respectively. Nevertheless, their scarcity and high price hinder their development and wide applications^{10–13}. Meanwhile, only a few OER catalysts (e.g. IrO₂ and RuO₂) are stable in acidic solutions, thus designing cost-effective and

earth-abundant bifunctional electrocatalysts with high efficiency of overall water splitting in the same alkaline conditions are of great significance and urgency^{7,14,15}.

Single-atom catalysts (SACs) featuring maximizing the atomic utilization rates and the synergistic effects between single-atom sites and its support are considered as the most promising strategy for designing cost-effective and earth-abundant bifunctional electrocatalysts^{16,17}. Currently, most SACs are based on carbonaceous substrates, such as amorphous carbon, graphene, with isolated metal atoms coordinated by intrinsic defects or heteroatoms. However, such catalysts show insufficient activity when applied in HER, especially in OER, while they exhibited obvious improvement in electrocatalytic O₂/CO₂ reduction reactions. So, it is a critical challenge to develop SACs with new highly conductive support. Transition metal-based carbides, such as molybdenum carbide (Mo₂C), had metal-like electric conductivity and received special attention as potential bifunctional

¹Key Laboratory of Cluster Science, Ministry of Education of China, Beijing Key Laboratory of Photoelectronic/Electrophotonic Conversion Materials, School of Chemistry and Chemical Engineering, Beijing Institute of Technology, Beijing 100081, China. ²Beijing Synchrotron Radiation Facility, Institute of High Energy Physics, Chinese Academy of Sciences, Beijing 100049, China. ³Engineering Research Center of Advanced Rare Earth Materials, Department of Chemistry, Tsinghua University, Beijing 100084, China. ⁴These authors contributed equally: Mengyun Hou, Lirong Zheng. ✉e-mail: dizhao@bit.edu.cn; caomh@bit.edu.cn; zhangjt@bit.edu.cn; cchen@mail.tsinghua.edu.cn

electrocatalysts for water splitting. However, the water-splitting catalytic performance of pure Mo₂C is far from satisfactory due to the weak adsorption strength of oxygen species and the slow dissociation kinetics of H₂ and other reaction intermediates^{18,19}. To address this challenge, one of the most effective strategies is to decorate with transition metals (Ni, Co, Pt, and W)^{20–22}. In addition, the bridging bond M₁-O-M₂ (M=metal) between the substrate material and single atoms can produce strong electronic coupling via the surface, resulting in effective charge transfer, which can optimize adsorption/desorption behavior of the active site for oxygen intermediates, hydrogen intermediates²³. For example, Suryanto group reported that the surface unique M₁-O-M₂ configuration could modify Gibbs free energy absorption of reaction intermediates (O* and OH*), then breaking the scale relationship and promoting OER and HER activities^{24–26}. So, it is feasible and challenging to construct atomically distributed metal centers on surface-oxygen-abundant Mo₂C to effectively modulate the adsorption/desorption behavior of the key intermediates during the water splitting process.

Furthermore, with insights into the electrocatalytic process, studies have evidenced that many electrocatalysts undergoes reconstitution during the so-called activation process or the initial cyclic voltammetry measurement. As for the HER example, Li et al. demonstrated that the V_o-Ru/HfO₂-OP occurred structural change during the HER activation process, resulting in high catalytic activity as well as stability²⁷. In addition, the Ni@Ni/NiO_x actual active sites for HER were generated by core@shell structure of Ni@O-Ni pre-electrocatalyst through the potential-driven reconstitution²⁸. Besides, Wang group had demonstrate that the active HER species of Co@CoFe-P NBs arose from in situ reconstructed P-Co-O-Fe-P configurations with low-valence metal sites (M⁰/Mⁿ), which can decrease the energy barriers for water dissociation and adsorption of H* intermediates²⁹. In sharp contrast, their OER activity arose from the oxygen-bridged, high-valence Co^{IV}-O-Fe^{IV} moieties. Due to the redox process in OER, the catalyst surface reconstitution is more likely to accompany. Most of the catalysts are fully oxidized into transition metal oxide or hydroxides, or their surfaces can be reconstructed into different coordination environments. Zhou et al. identified that the CoNi_{0.5}P catalyst was transformed into the low-crystalline CoNi_{0.25}O_x(OH)_y during the OER process and found that the CoNi_{0.25}O_x(OH)_y serve as the reactive species for OER rather than the original CoNi_{0.5}P species³⁰. Meanwhile, Li group reported the reconstitution of WC_x-FeNi catalysts, that is, O-bridged FeNi moieties were formed after electrochemical treatment, which provided the high oxygen-evolving catalytic activity³¹. All the pioneering works mentioned above have demonstrated, that the ability of the catalyst to “evolve” during the reaction may be a key feature of highly active OER catalysts. So, understanding of the structural transformation of the catalysts is crucial to better unveil the real catalytic mechanism and design novel electrocatalysts, although they have rarely been studied for SACs³².

Here, we primarily motivated to use Mo₂C with the partially oxidized surface as a support material to stabilize Ni single atoms. The resulting materials possess a thin layer of atomic Ni sites, which interacted with the oxidized surface of Mo₂C via Ni-O-Mo bridge bonds (Ni_{SA}-O/Mo₂C) and exhibited good catalytic activity for HER, OER, and overall water splitting. By ex situ synchrotron X-ray absorption spectroscopy and electron microscopy observations, we found, the configuration of atomically dispersed Ni in Ni_{SA}-O/Mo₂C electrocatalyst underwent transformation and O/Mo₂C support were overoxidized or dissolved to varying degrees. After HER, the coordination number of Ni-O and the bond length of Ni-Mo (Ni-O-Mo) were all increased, but Ni species still remained atomically dispersed form. However, after OER, the coordination number of Ni-O increased, the coordination number of Ni-Mo (Ni-O-Mo) decreased but new Ni-Ni (Ni-O-Ni) bonds appeared, indicating the atomically dispersed Ni were agglomerated into very small clusters

under applied potentials. Combining the experimental results and DFT calculations, we found partially oxidized Mo₂C will be beneficial to HER performance. However, compared with the original Ni_{SA}-O/Mo₂C, the potential-driven reconstituted small Ni clusters with optimal Ni-O, Ni-Mo and Ni-Ni coordination structures are more conducive to catalyzing the production of O₂.

Results

Material synthesis and characterization

The Ni_{SA}-O/Mo₂C nanospheres were synthesized by the following steps: (1) preparation of Mo-based organic nanosphere precursors by a facile hydrothermal method; (2) adsorption of the Ni metal ions via impregnation method; (3) heat treatment at certain temperatures under air and H₂/Ar atmospheres. During the pyrolysis process, the Mo-based organic precursors were simultaneously converted to Mo₂C nanocrystals with Ni ions fixed on their surfaces, which embedded in a uniform carbon substrate. Transmission electron microscopy (TEM) images of Fig. S1 shows that the amorphous Mo-based precursor is a nanosphere structure with rough surfaces with a diameter of about 200 nm, and the morphology does not change significantly after the adsorption of Ni ions on the surface (Fig. S2). After pyrolysis, an obvious double-shelled hollow structure can be observed (Fig. 1a, b). The mechanism of double-shelled hollow structure formation has been studied in detail (Figs. S3–S6) and its possible schematic illustration is shown in Fig. S7, which is mainly based on the early oxidation of air and non-equilibrium non-uniform shrinkage caused by heat treatment^{33,34}. During the formation of double-shelled hollow structure, the conditions of air and H₂/Ar atmospheres are both vitally important. In addition, the specific surface areas obtained from N₂ adsorption-desorption isotherms show a significant increase from 13.9 for O/Mo₂C to 64.3 m² g⁻¹ for Ni_{SA}-O/Mo₂C (Fig. S8), which is probably due to the volatilization of nitrate from Ni sources. X-ray diffraction (XRD) patterns (Fig. S9) indicate that the diffraction of Ni_{SA}-O/Mo₂C can be well indexed to pure Mo₂C phase (JCPDS card no.35-0787)³⁵. No peaks of Ni metals, metal oxide can be observed. The selected area electron diffraction (SAED) pattern (insert in Fig. 1b) indicates the polymorphism of the Ni_{SA}-O/Mo₂C.

Energy-dispersive X-ray spectroscopy (EDS) mapping images reveal that Mo, Ni, and O elements almost have the same double-shelled hollow shape and C elements is uniformly distributed in an individual Ni_{SA}-O/Mo₂C nanospheres (insert in Fig. 1c, and Fig. 1d). Combined with the HR-TEM magnified image in Fig. S10, we further confirm that Mo₂C nanocrystals with Ni ions were embedded in a uniform carbon substrate. To further identify the exact location of single Ni atoms in the Mo₂C nanospheres, we performed sub-angstrom-resolution high-angle annular dark field aberration-corrected (HAADF)-scanning TEM (STEM) (Fig. 1e, f). Figure 1e clearly detected the lattice fringes with an interplanar distance of 0.228 nm and 0.135 nm, corresponding to the (101) and (103) plane of a hexagonal β-Mo₂C, respectively. Detailed observation of the edge of the bright Mo atom array reveals an amorphous or low crystallinity molybdenum oxide (MoO_x) layer (around the yellow line in Fig. 1f) due to surface oxidation^{36,37}. In addition, due to the different Z-contrast, the darker spots (red circles in Fig. 1f) on the edge of brighter spots (Mo atoms) can be identified as isolated Ni single atoms³⁸. The intensity profiles at the location of position g1 and g2 marked by yellow circles in Fig. 1f including darker spots and brighter spots of surface MoO_x layer further confirm the presence of isolated Ni_{SA} single atoms (Fig. g1 and g2)⁸. For comparison, the control electrocatalysts of Ni_{1.5}-O/Mo₂C and Ni_{4.5}-O/Mo₂C were prepared with varying amounts of Ni. XRD patterns and TEM images display the same crystal structure and morphologies as those of Ni_{SA}-O/Mo₂C (Figs. S9, S11). Their Ni-loading contents detected by inductively coupled plasma atomic emission spectroscopy (ICP-AES) are 0.75 wt%, 0.98 wt% and 1.33 wt%, respectively (Table S1).

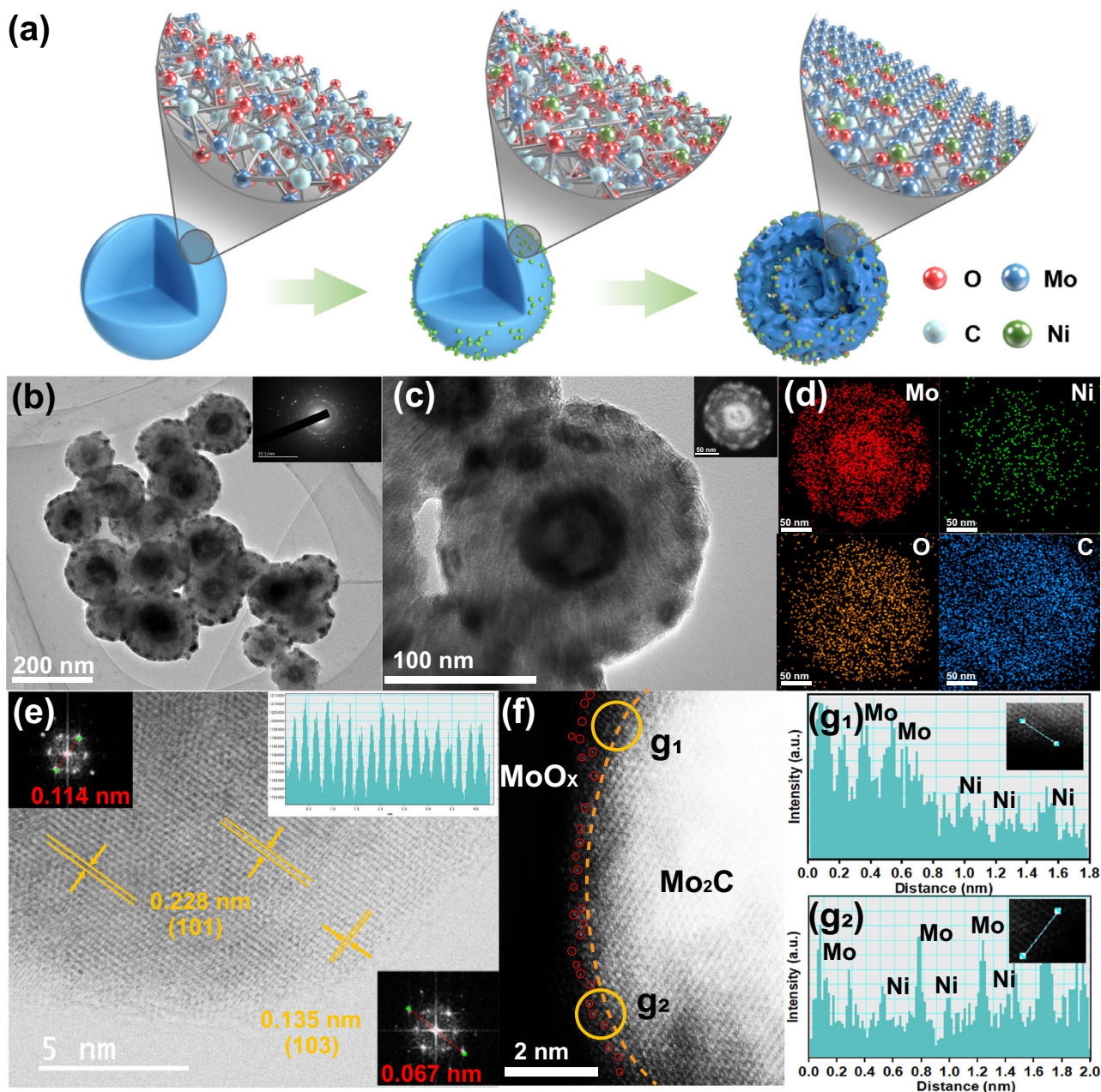


Fig. 1 | Morphology and structure of the materials. **a** Schematic illustration of the fabrication process of the $\text{Ni}_{\text{SA}}\text{-O}/\text{Mo}_2\text{C}$ electrocatalyst. **b, c** HR-TEM image of $\text{Ni}_{\text{SA}}\text{-O}/\text{Mo}_2\text{C}$. Insets in **(b)**: SAED pattern. **d** Elemental mapping of Mo, Ni, O, C for an individual $\text{Ni}_{\text{SA}}\text{-O}/\text{Mo}_2\text{C}$ nanospheres (inset in Fig. 1c), respectively. **e** HAADF-STEM

image and **f** corresponding enlarged view of the $\text{Ni}_{\text{SA}}\text{-O}/\text{Mo}_2\text{C}$. The bright dots highlighted with red in **(f)** marks the Ni single-atoms in $\text{Ni}_{\text{SA}}\text{-O}/\text{Mo}_2\text{C}$. **g** Lineal contrast analysis for selected area of g_1 and g_2 at the edge of Fig. 1f.

Since the coordination environment determines the electronic structure, the valence states of Mo, and Ni have been studied by X-ray photoelectron spectroscopy (XPS) (Figs. S12-13). As shown in Fig. 2a, the high-resolution Mo $3d$ spectra of pure Mo_2C were deconvoluted into six peaks, corresponding to Mo^{2+} (228.6 eV, 231.7 eV), Mo^{4+} (229.0 eV, 232.0 eV) and Mo^{6+} (232.8 eV, 235.8 eV) species³⁹. Mo^{4+} and Mo^{6+} can be assigned to molybdenum oxides due to surface oxidation of Mo species, indicating a thin surface layer of MoO_x were formed outside Mo_2C electrocatalyst (denoted as $\text{O}/\text{Mo}_2\text{C}$)³⁷. This is well consistent with HAADF-STEM analysis (Fig. 1e-f). It is worth mentioning that, the surface oxide layer can be controlled by the atmosphere and temperature to which the $\text{Ni}_{\text{SA}}\text{-O}/\text{Mo}_2\text{C}$ is exposed. For example, when the newly reduced $\text{Ni}_{\text{SA}}\text{-O}/\text{Mo}_2\text{C}$ were taken out of the tube furnace at 60 °C in air, its surface would be much more oxidized compared with the main sample of $\text{Ni}_{\text{SA}}\text{-O}/\text{Mo}_2\text{C}$. While, when the newly reduced $\text{Ni}_{\text{SA}}\text{-O}/$

Mo_2C were protected in Ar atmosphere for 12 h before taking out the furnace, its surface would be much lower oxidized compared with the main sample of $\text{Ni}_{\text{SA}}\text{-O}/\text{Mo}_2\text{C}$. (Fig. S13a, b). In addition, after etching the surface oxide layer, the main phase of Mo_2C gradually leaks out, which is demonstrated by XPS results with different etching depths (Fig. 2a, Fig. S13c). The XPS spectrum of C $1s$ (Fig. S14a) is fitted into four different signals at 283.9, 284.8, 285.8, and 288.9 eV, which are attributed to C-Mo, C-C/C=C, C-O, and O-C=O, respectively³⁷. After loading of Ni atoms, the binding energy of Mo $3d$ XPS spectra for $\text{Ni}_{\text{SA}}\text{-O}/\text{Mo}_2\text{C}$ display a positive shift about 0.12 eV compared with that of pure $\text{O}/\text{Mo}_2\text{C}$, indicating the charge migration caused by the atomic Ni incorporation¹³. This is further proved by the positive shift of the main peak of O XPS for $\text{Ni}_{\text{SA}}\text{-O}/\text{Mo}_2\text{C}$ compared with that of pure $\text{O}/\text{Mo}_2\text{C}$ (Fig. S14b). The Ni $2p$ XPS spectrum can be split into six peaks, of which the peaks at 856.4 and 874.2 eV are assigned to Ni^{2+} caused by the

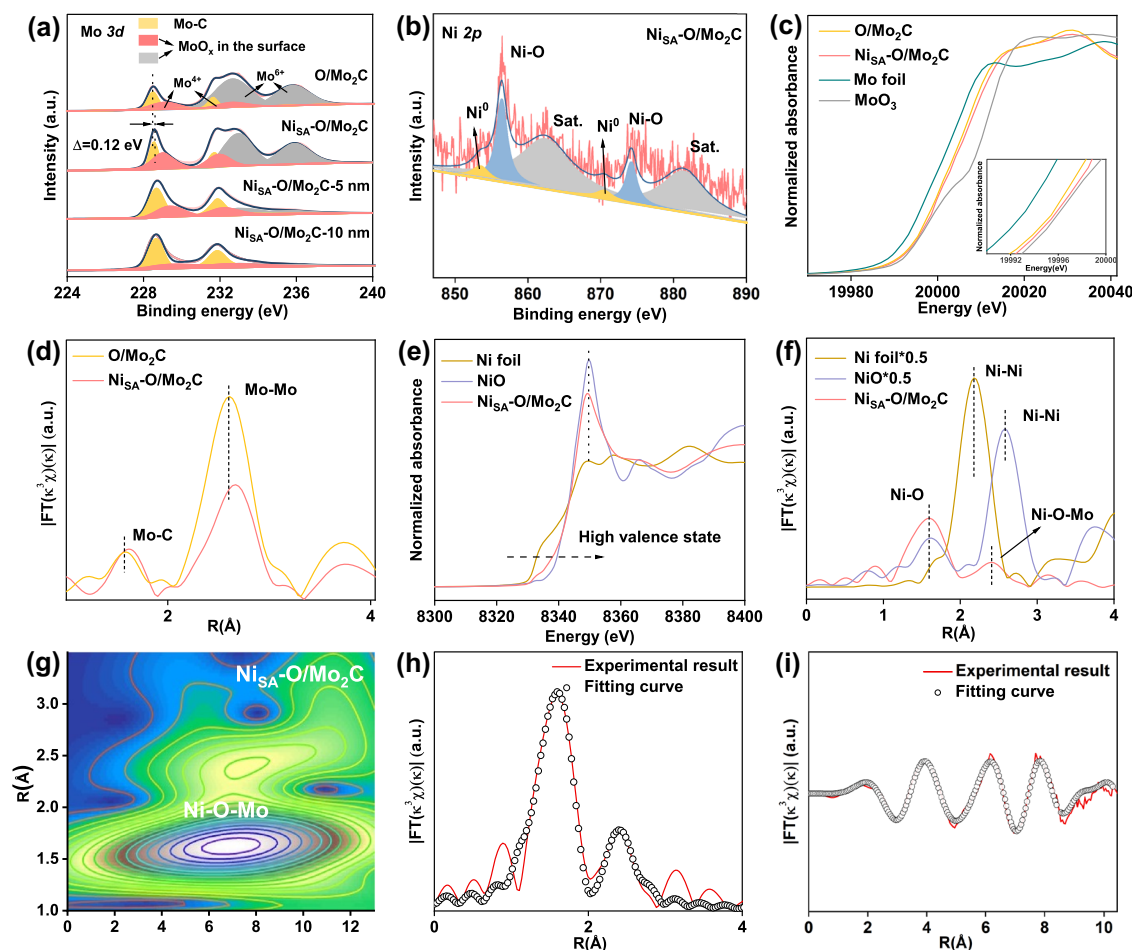


Fig. 2 | Structural characterization. **a** XPS spectra of Mo 3d. **b** XPS spectra of Ni 2p. **c** Mo K-edge XANES spectra. Inset in (c) is the partial enlargement of the pre-edge peak. **d** The FT-EXAFS curves for the as-prepared samples. **e** Ni K-edge spectra. **f** The corresponding FT-EXAFS curve. **g** The wavelet transform (WT) of the Ni_{SA}-O/Mo₂C. **h, i** Ni K-edge EXAFS of Ni_{SA}-O/Mo₂C in R and k spaces.

bonding between Ni and adsorbed oxygen, and the peaks at 862.4 and 881.4 eV correspond to the satellite peaks of Ni (Fig. 2b). Only a small amount of Ni⁰ can be observed at 853.5 and 870.5 eV, which indicates that the Ni atoms are mainly coordinated with the surrounding oxygen atoms⁸. It should be noted that, due to the Ni content in the Ni_{1.5}-O/Mo₂C is lower than Ni_{SA}-O/Mo₂C, the peak of Ni⁰ is not obvious, while Ni²⁺ is observed at 862.4 and 881.4 eV, indicating that Ni in the Ni_{1.5}-O/Mo₂C sample is almost entirely bonded to the surrounding oxygen atoms. While, the proportion of Ni⁰ peak in Ni_{4.5}-O/Mo₂C is significantly larger than that in Ni_{SA}-O/Mo₂C (Fig. S15), which is probably due to the excessive Ni aggregates into Ni clusters or nanoparticles.

To assess the electronic structure and local environment of the Ni and Mo in Ni_{SA}-O/Mo₂C, X-ray absorption near-edge spectroscopy (XANES) and extended X-ray absorption fine structure (EXAFS) were investigated. The Mo K-edge XANES spectra are shown in Fig. 2c. Compared with pure O/Mo₂C, the pre-edge of Ni_{SA}-O/Mo₂C was higher, suggesting that the average oxidation state of Mo in the Ni_{SA}-O/Mo₂C was more positive, which is consistent with the aforementioned XPS results. The Fourier transform (FT) extended EXAFS (Fig. 2d) of the pure O/Mo₂C and Ni_{SA}-O/Mo₂C possessed two peaks. The strongest peak is located at -2.6 \AA , corresponding to the Mo-Mo bonds. The other peak is located at -1.6 \AA , which is associated with the Mo-C bonds³⁵. Compared with pure O/Mo₂C, the introduction of Ni would extend the Mo-Mo and Mo-C bonding length due to the interaction between Ni and Mo₂C. The Ni K-edge pre-edge of Ni_{SA}-O/Mo₂C is located between the Ni and NiO (Fig. 2e), which indicates that the valence of Ni in Ni_{SA}-O/Mo₂C is

situated between 0 and +2. The Ni K-edge XANES spectra and the corresponding k-space spectra of Ni_{SA}-O/Mo₂C closely resemble that of NiO reference (Fig. S16), suggesting the formation of surface Ni-O³⁶. The Fourier transformed (FT) k^3 -weighted EXAFS spectrum in R space further confirmed the formation of Ni-O on the amorphous thin layer MoO_x on the surface of Mo₂C. As shown in Fig. 2f, one notable peak at -1.58 \AA contributed by the Ni-O peak is observed. The FT $k^3\chi(k)$ of Ni foil shows a peak at $\sim 2.18 \text{ \AA}$ and NiO displays a peak at $\sim 2.58 \text{ \AA}$, both corresponding to the Ni-Ni interaction. Ni_{SA}-O/Mo₂C does not have these peaks, which demonstrates that Ni atoms should exist in the single-atomic form on the amorphous thin layer MoO_x. In addition, there is a scattering peak at around 2.4 \AA , which could be due to the bonding of Ni-Mo. Combined with aforementioned results of the oxidized surface of Ni_{SA}-O/Mo₂C, Ni-O-Mo bonding should dominate on the surface.

We have also performed wavelet transform (WT) analysis of Ni_{SA}-O/Mo₂C for verifying the coordination environments of Ni-O-Mo bonding, which allows information to be displayed in both R-space and K-space. As shown in Fig. 2g, a strong WT signal focused at 6.91 \AA^{-1} , which was derived from Ni-O-Mo contribution. To acquire the precise coordination configuration of Ni atoms in Ni_{SA}-O/Mo₂C, the quantitative EXAFS fitting is performed to extract the structural parameters and the results are presented in Fig. 2h, i and summarized in Table S3. The best-fitted result reveals Ni atom is coordinated with O with a coordination number of 3.9 at 2.01 \AA and as well coordinated with Mo with a coordination number of 5.0 at 2.98 \AA in the second or higher shell. In addition, the Ni_{4.5}-O/Mo₂C with higher Ni content has a weak

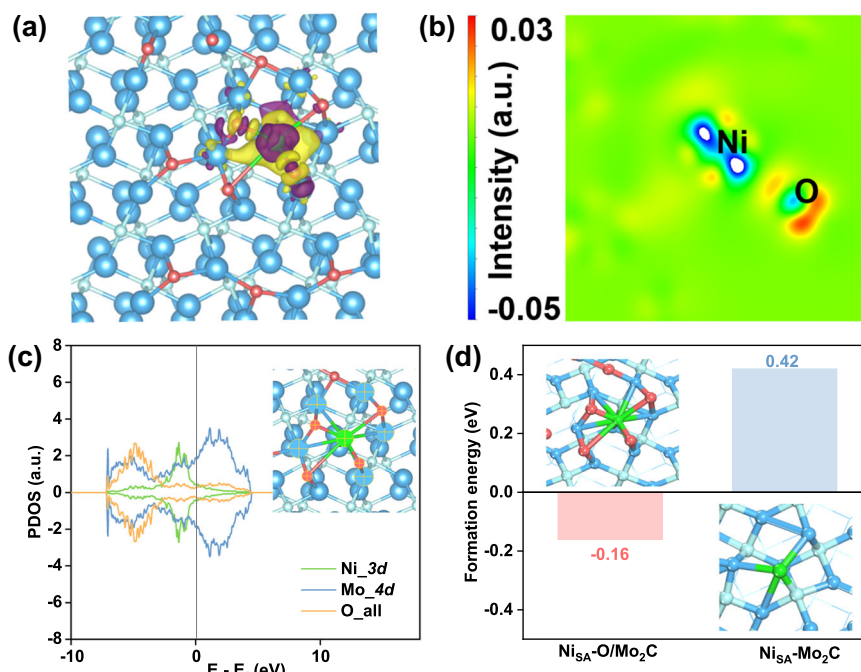


Fig. 3 | DFT calculation. The two plots of charge density differences of Ni_{SA}-O/Mo₂C: top view of 3D plot (a) and 2D display (b). The isosurface level set to 0.003 eÅ⁻³, where charge depletion and accumulation were depicted by purple and

yellow, respectively. **c** PDOS graph of 3d orbitals of Ni, 4d orbitals of Mo, and all orbitals of O atoms specified by cross marks in Ni_{SA}-O/Mo₂C. **d** The chemisorption energies of Ni atom on surfaces of Ni_{SA}-O/Mo₂C and Ni_{SA}-Mo₂C.

peak at 2.18 Å corresponding Ni-Ni signal (Fig. S17), which is well consistent with the results of XPS.

In order to further study the mechanism of Ni atoms binding on the oxygen-incorporated Mo₂C, we did a series of DFT calculations. According to the previous results of structural analysis, we chose plane (101) of Mo₂C as the reaction surface. Then, calculations were made on the absorption of oxygen atoms on the surface, and we determined the most stable structure (Fig. S18) by comparing the values of their total energy. So, we attached some oxygen atoms to the facet by the most solid adsorption to simulate a partially oxidized surface of O/Mo₂C. According to the above data, we adsorbed Ni atom bonding with four oxygen atoms and one carbon atom at the facet, respectively, to obtain calculation models Ni_{SA}-O/Mo₂C and Ni_{SA}-Mo₂C (Fig. S19). Firstly, we performed calculations of the charge density difference between Ni and facet, as shown in Fig. 3a, b. It could be clearly seen that obvious tendency to transfer electrons from Ni site to surrounding atoms, indicating the interaction between Ni with facet. This is also confirmed by Fig. 3c, because of overlaps between the orbitals of Ni, O, and Mo atoms (marked by cross) around the Fermi level. So, we concluded that Ni atoms could be stably adsorbed on the partially oxidized facet of Mo₂C. In addition, the value of adsorption energy at Ni_{SA}-O/Mo₂C (-0.16 eV) was significantly lower than Ni_{SA}-Mo₂C (0.42 eV) (Fig. 3d), further indicating that the bonding of Ni-O-Mo was more stable.

Electrocatalytic performance

To examine the electrochemical OER catalytic activities in 1 M KOH using a three-electrode set-up. As shown in Fig. 4a, the Ni_{SA}-O/Mo₂C exhibits an overpotential (η) of 299 mV at 10 mA cm⁻², which significantly exceeds those of Ni_{1.5}-O/Mo₂C (379 mV), Ni_{4.5}-O/Mo₂C (337 mV), pure O/Mo₂C (547 mV) and commercial IrO₂ catalyst (386 mV). From these η values, we can see that the higher loadings of Ni results in better performance due to the higher density of catalytic reactive centers. However, the catalysts cannot perform even better when the Ni loading is excessive. In addition, the overpotential of Ni_{SA}-O/Mo₂C catalyst requires only 430 mV at the current density of 200 mA cm⁻², even far less than 670 mV required by commercial IrO₂ catalyst,

demonstrating a huge improvement of the OER activity under the high current density. In addition, Fig. 4a shows the Ni oxidation peak, corresponding to the oxidation Ni from low valence states (Ni⁰) to high valence states (Ni²⁺/Ni³⁺)²⁴. Tafel slopes were calculated to unveil that Ni_{SA}-O/Mo₂C endows a smaller Tafel slope (89.36 mV dec⁻¹), much lower than those of Ni_{1.5}-O/Mo₂C (99.89 mV dec⁻¹), Ni_{4.5}-O/Mo₂C (95.22 mV dec⁻¹), pure O/Mo₂C (176.28 mV dec⁻¹) and even commercial IrO₂ (155.77 mV dec⁻¹), which is a sign of its fast electron transfer and superior mass transport properties (Fig. 4b)³¹. Motivated by the promising OER performance of Ni_{SA}-O/Mo₂C, the electrocatalytic HER was also investigated in the same 1.0 M KOH environment. Figure 4c shows the Pt/C catalyst exhibits the best HER activity, whereas Ni_{SA}-O/Mo₂C shows competitive performance with an overpotential of 133 mV at a current density of 10 mA cm⁻², which is lower than those of Ni_{1.5}-O/Mo₂C (163 mV), Ni_{4.5}-O/Mo₂C (143 mV) and pure O/Mo₂C (182 mV). Furthermore, the Tafel slope of the Ni_{SA}-O/Mo₂C is 83.6 mV dec⁻¹, less than those of Ni_{1.5}-O/Mo₂C (93.64 mV dec⁻¹), Ni_{4.5}-O/Mo₂C (92.36 mV dec⁻¹) and pure O/Mo₂C (121.59 mV dec⁻¹) (Fig. 4d). It is worth noting that in order to exclude the role of Ni atoms on carbon substrate, we set up two control samples: Ni atoms on carbon substrate obtained via etching Mo₂C particles in Ni_{SA}-O/Mo₂C (Ni_{SA}/C_{etch}) and Ni atoms on pure carbon spheres (Ni/C) synthesized by the same method with Ni_{SA}-O/Mo₂C. As can be seen from XRD patterns, TEM, and element mappings (Fig. S20), both samples only show carbon peaks and uniform Ni element distribution. Electrochemical tests showed that compared with Ni_{SA}-O/Mo₂C, their HER and OER catalytic activity can be ignored (Fig. S21), indicating the catalytic activity of Ni_{SA}-O/Mo₂C comes from the Ni single atoms anchored on oxygen-incorporated Mo₂C. Impressively, Ni_{SA}-O/Mo₂C outperformed most of the non-precious metal SACs in alkaline media (Fig. 4e, Tables S4-5), proving Ni_{SA}-O/Mo₂C is a potentially highly efficient bifunctional catalyst. To investigate the electrode kinetics under the catalyst process, electrochemical impedance spectroscopy (EIS) measurements were carried out. Fig. S22 displays a favorable charge transfer resistance (R_{ct}) of Ni_{SA}-O/Mo₂C (R_{ct} =12 Ω) as compared with other control samples⁴⁰. Besides, the electrochemical active surface area (ECSA) of all samples was

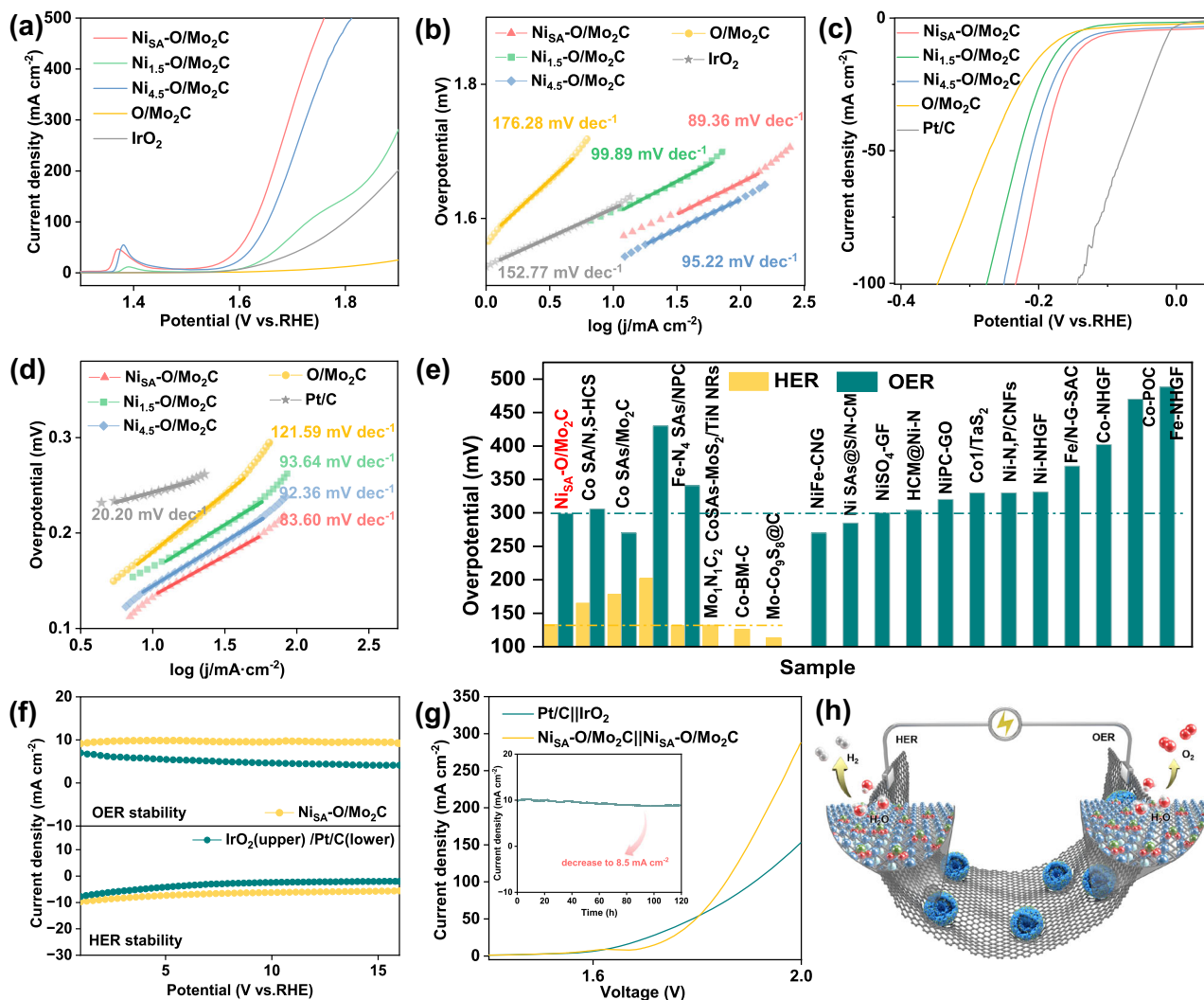


Fig. 4 | HER, OER and overall water splitting performance of the $\text{Ni}_{\text{SA}}\text{-O}/\text{Mo}_2\text{C}$ catalyst in 1.0 M KOH (pH=14) with iR compensation. **a** Polarization curves and **b** Tafel plots for $\text{Ni}_{\text{SA}}\text{-O}/\text{Mo}_2\text{C}$, $\text{Ni}_{1.5}\text{-O}/\text{Mo}_2\text{C}$, $\text{Ni}_{4.5}\text{-O}/\text{Mo}_2\text{C}$ and pure $\text{O}/\text{Mo}_2\text{C}$, commercial IrO_2 for OER (loading amount 0.74 mg cm^{-2}). **c** Polarization curve and **d** Tafel plots for $\text{Ni}_{\text{SA}}\text{-O}/\text{Mo}_2\text{C}$, $\text{Ni}_{1.5}\text{-O}/\text{Mo}_2\text{C}$, $\text{Ni}_{4.5}\text{-O}/\text{Mo}_2\text{C}$ and pure $\text{O}/\text{Mo}_2\text{C}$, 20% Pt/C for HER (loading amount 0.7 mg cm^{-2}). **e** Comparison of the overpotentials of $\text{Ni}_{\text{SA}}\text{-O}/\text{Mo}_2\text{C}$ and recently reported non-precious metal SACs at 10 mA cm^{-2} in 1.0 M

KOH. The histograms in yellow and green denote the HER, OER performance, respectively. **f** Current density versus time (i-t) curves for HER and OER. **g** Polarization curves of $\text{Ni}_{\text{SA}}\text{-O}/\text{Mo}_2\text{C}||\text{Ni}_{\text{SA}}\text{-O}/\text{Mo}_2\text{C}$ and Pt/C|| IrO_2 couples for overall water splitting in 1.0 M KOH (loading amount 0.74 mg cm^{-2}). Inset **g** is the long-term durability of overall water splitting at a current density of 10 mA cm^{-2} . **h** Illustration of the $\text{Ni}_{\text{SA}}\text{-O}/\text{Mo}_2\text{C}$ electrodes for overall water splitting.

reflected from the double layer capacitance (C_{dl}) (Fig. S23). $\text{Ni}_{\text{SA}}\text{-O}/\text{Mo}_2\text{C}$ catalyst has the highest C_{dl} value, which indicates that $\text{Ni}_{\text{SA}}\text{-O}/\text{Mo}_2\text{C}$ has more exposed active surface area than other samples. Since the specific activity reflects the intrinsic activity of the catalysis, ECSA-normalized LSV curves for both HER and OER were shown in Fig. S24. The specific activity (SA) normalized by ECSA shows that $\text{Ni}_{\text{SA}}\text{-O}/\text{Mo}_2\text{C}$ exhibits the best electrocatalytic activity toward both OER and HER compared to other catalysts following the order of $\text{Ni}_{\text{SA}}\text{-O}/\text{Mo}_2\text{C} > \text{Ni}_{4.5}\text{-O}/\text{Mo}_2\text{C} > \text{Ni}_{1.5}\text{-O}/\text{Mo}_2\text{C} > \text{O}/\text{Mo}_2\text{C}$. In particular for OER, at the overpotential of 370 mV (Fig. S24d), $\text{Ni}_{\text{SA}}\text{-O}/\text{Mo}_2\text{C}$ exhibits the SA of $8.71 \text{ mA cm}^{-2}_{\text{ECSA}}$, which is higher than those of $\text{Ni}_{4.5}\text{-O}/\text{Mo}_2\text{C}$ ($4.67 \text{ mA cm}^{-2}_{\text{ECSA}}$), $\text{Ni}_{1.5}\text{-O}/\text{Mo}_2\text{C}$ ($2.26 \text{ mA cm}^{-2}_{\text{ECSA}}$) and $\text{O}/\text{Mo}_2\text{C}$ ($0.52 \text{ mA cm}^{-2}_{\text{ECSA}}$). These results indicate incorporation of Ni not only improves the density of active sites but also intrinsically improves HER and especially OER activity of $\text{Ni}_{\text{SA}}\text{-O}/\text{Mo}_2\text{C}$ catalyst. The durability of the catalyst is an important indicator, especially for SACs. For OER, long-term electrolysis at a constant current has been performed under a constant current of 10 mA cm^{-2} by chronoamperometry for 16 h (Fig. 4f), which proved that the currents of $\text{Ni}_{\text{SA}}\text{-O}/\text{Mo}_2\text{C}$ first increase and then maintain stability for a long time. In contrast, after 16 h, the

commercial IrO_2 catalyst shows distinctly difference in the required overpotential. For HER, although it was much more stable than 20 wt % Pt/C, the current density of the $\text{Ni}_{\text{SA}}\text{-O}/\text{Mo}_2\text{C}$ catalyst decreased slightly after 16 h.

Furthermore, we assembled an electrolyzer with 1.0 M KOH electrolyte using $\text{Ni}_{\text{SA}}\text{-O}/\text{Mo}_2\text{C}$ as bifunctional electrodes ($\text{Ni}_{\text{SA}}\text{-O}/\text{Mo}_2\text{C}||\text{Ni}_{\text{SA}}\text{-O}/\text{Mo}_2\text{C}$). Pt/C|| IrO_2 was also tested for comparison. Figure 4g gives a comparison of LSV curves of $\text{Ni}_{\text{SA}}\text{-O}/\text{Mo}_2\text{C}||\text{Ni}_{\text{SA}}\text{-O}/\text{Mo}_2\text{C}$ and Pt/C|| IrO_2 . The cell voltage required to reach 10, 100, and 150 mA cm^{-2} for $\text{Ni}_{\text{SA}}\text{-O}/\text{Mo}_2\text{C}$ are 1.69 V, 1.86 V, and 1.90 V, while Pt/C|| IrO_2 requires 1.64 V, 1.91V and 1.93V, respectively. The result shows that the electrocatalytic overall splitting performance of $\text{Ni}_{\text{SA}}\text{-O}/\text{Mo}_2\text{C}||\text{Ni}_{\text{SA}}\text{-O}/\text{Mo}_2\text{C}$ is comparable to that of Pt/C|| IrO_2 especially under the high current density and superior to most reported single-atom catalysts (Table S6). In the stability test, the current density has only decreased from 10 mA cm^{-2} to 8.5 mA cm^{-2} after 120 h, indicating its good stability as a bifunctional electrocatalyst (inset in Fig. 4g). Moreover, the obvious bubbles were observed at the cathode and anode in the long-time stability testing, corresponding to H_2 and O_2 , respectively (Fig. 4h and Fig. S25).

Potential-driven new active interfaces generation

In order to reveal the different stability phenomena of HER and OER, a series of characterizations were carried out to probe the identity of the real catalytically active species. The XRD pattern (Fig. S26a) indicates that the surface of Ni_{SA}-O/Mo₂C undergoes structural reorganization to form different phases after the different electrochemical reactions. After electrochemical HER, the Ni_{SA}-O/Mo₂C catalyst maintains the diffraction peaks of Mo₂C, but other weaker peaks of MoO₃ (JCPDS card no.35-0609) and MoO₄²⁻ (JCPDS card no.29-1021) appear. In contrast, for OER, all the XRD peaks could be assigned to the crystal structures of MoO₃ (JCPDS card no. 05-0508 and 35-0609) and MoO₄²⁻ without Mo₂C peaks, indicating the Mo₂C were completely disintegrated. Fig. S27 shows the Mo 3d spectra of Ni_{SA}-O/Mo₂C after reactions, the major Mo peaks can be assigned to Mo⁶⁺ without low valence state of Mo, suggesting the average oxidation state of Mo are both higher than that of Ni_{SA}-O/Mo₂C, that is to say the surface of the catalysts both have obvious oxidation behavior^{41,42}. However, after HER reaction, the Mo⁶⁺ peak shifted to a little lower position, which is probably due to the interaction between single atom Ni and the reconstructed substrate. The morphology of double-shelled hollow structure was not obviously changed after catalytic reactions (Fig. S28-30). However, in the case of Ni_{SA}-O/Mo₂C after HER, the enlarged HRTEM image shows original large Mo₂C nanoparticles were crushed into smaller ones and two different lattices of 0.22 nm and 0.23 nm correspond to the d-spacing of (101) and (060) planes of the Mo₂C and MoO₃, respectively (Fig. 5a, b). Besides, in the Ni_{SA}-O/Mo₂C after OER, the image exhibits the big Mo₂C nanoparticles were changed obviously to smaller ones and the interplanar spacings of 0.21 and 0.23 nm correspond to the (141) and (060) plane of MoO₃. These results indicate that Ni_{SA}-O/Mo₂C undergoes reconstitution in the process of HER and OER. So, in order to determine the real active species involved in these two reactions, ex-situ XANES and FT-EXAFS spectra after CV and i-t chronoamperometric test for HER and OER were further recorded. As displayed in Fig. 5c, the Mo K-edge XANES spectra for catalysts after HER and OER activation show both positive shifts in the absorption edge compared with that of Ni_{SA}-O/Mo₂C, indicating the valences Mo oxidation states were increased. However, for catalysts after OER, the Mo K-edge XANES spectra show more positive shifts compared with that of catalysts after HER, indicating catalysts after OER has higher valence state of Mo, which consistent with XPS results. In addition, a new notable shoulder peak in the pre-edge region of OER were shown, suggesting the formation of strongly distorted MoO₆ octahedra. Figure 5d,e show the Mo k³-weighted FT-EXAFS spectra of Ni_{SA}-O/Mo₂C after HER and OER, respectively. After HER, it shows the main peak centered at -2.6 Å, corresponding to the Mo-Mo scattering in Mo₂C. In particular, two smaller peaks located at around 1.3 Å and 0.88 Å can be found, which are typical characteristic of Mo-O bonds, indicating the surface of Mo₂C was further oxidized^{39,40}. In contrast, after OER, the spectra display the existence of the Mo-O bond but no Mo-Mo bond, and its shape is similar with that of molybdate, indicating, except for crystal MoO₃, amorphous or low crystallinity molybdate was also formed followed by the possible reaction of MoO₃ + OH⁻= MoO₄²⁻ + H₂O⁴³⁻⁴⁵. In order to clarify whether the changes of Ni_{SA}-O/Mo₂C is automatic in KOH KOH electrolyte at open circuit potential (OCP). As shown in Fig. conditions, we tested the XRD, Mo k-edge XANES and FT-EXAFS curve for Ni_{SA}-O/Mo₂C electrocatalysts after being dipped into KOH electrolyte at open circuit potential (OCP). As shown in Fig. S26b, the Ni_{SA}-O/Mo₂C electrocatalysts after being dipped into KOH electrolyte at OCP (Ni_{SA}-O/Mo₂C-OCP) has similar characteristic peaks with Ni_{SA}-O/Mo₂C after HER except the a little weaker MoO₃ and MoO₄²⁻ peaks. Based on the dissolution of MoO_x in KOH⁴³⁻⁴⁵, we speculate the original surface MoO_x reacts with KOH to form MoO₄²⁻, and with the consumption of surface MoO_x, Mo₂C surface is continuously oxidized to form new surface MoO_x until the Mo₂C is completely dissolved in KOH. However, compared with Ni_{SA}-O/Mo₂C after OER, Ni_{SA}-O/

Mo₂C-OCP has characteristic peaks of Mo₂C. In addition, compared with Ni_{SA}-O/Mo₂C and Ni_{SA}-O/Mo₂C after HER, the absorption edge of Ni_{SA}-O/Mo₂C-OCP was higher, suggesting its average oxidation state of Mo was more positive. Meanwhile, the Mo k-edge XANES shape and the Mo k³-weighted FT-EXAFS spectra of Ni_{SA}-O/Mo₂C-OCP are different from Ni_{SA}-O/Mo₂C after HER but similar with that of Ni_{SA}-O/Mo₂C after OER. These results indicate the dissolution and oxidation of Mo₂C in KOH is automatic in alkaline conditions. The applied oxidation potential of OER process will intensify these two continuous reaction processes, while HER process will inhibit to a certain extent the oxidation of the inner layer of Mo₂C and then partially prevent the formation of MoO₄²⁻ from the outer layer of MoO_x. Based on the dissolution of MoO_x in KOH, Fig. 5f, g present comparisons of Ni_{SA}-O/Mo₂C catalysts in Ni K-edge XANES and FT-EXAFS after HER and OER. In the case of HER (Fig. 5f), the pre-edge position of XANES spectra show a slight shift to higher energy values compared with the original Ni_{SA}-O/Mo₂C, indicating that the Ni oxidation state slightly increases but still between Ni⁰ and Ni²⁺. After carefully compared the FT-EXAFS spectra of Ni_{SA}-O/Mo₂C before and after HER, we found the peak of Ni-O did not change, however the position of Ni-O-Mo was shift to higher R, which due to the reconstitution of Mo₂C substrate. After EXAFS fitting, we found the distance of Ni-O (2.05 Å) is almost the same as that of Ni_{SA}-O/Mo₂C (2.01 Å) and Ni-Mo (Ni-O-Mo) is increased from 2.40 to 3.31 Å (Table S7). Moreover, the Ni-O coordination number increased to 5.90 while the Ni-Mo decreased to 4.50. And no typical peaks for Ni-Ni bonds are observed as well. These results indicated the Ni was still exists as single atoms while its coordination structure had changed slightly. This catalyst after HER was collectively denoted as Ni_{SA}-Mo_x/Mo₂C. In contrast, after OER (Fig. 5g), the position of the absorption edge is higher than that of the Ni(OH)₂ reference, indicating the Ni has the higher oxidation than +2, which probably due to the existence of NiOOH or the strong electron interaction between Ni(OH)₂ and the reconstructed substrate (Fig. S31). For the FT-EXAFS spectra of the Ni K-edge after OER, these shapes match well with that of Ni(OH)₂. In addition, the Ni-O-Mo coordinated peak almost disappears and new distinct scattering of Ni-Ni emerges at -2.7 Å. The corresponding fitting EXAFS results display the bond distances Ni-O if 2.05 Å, Ni-Ni (Ni-O-Ni) is 3.07 Å and Ni-Mo (Ni-O-Mo) is 3.34 Å, respectively. The HAADF-STEM images (Fig. 5h) demonstrate the (060) plane of crystal MoO₃ and a smaller nanocluster of Ni (yellow circles). In addition, the selected-area elemental mappings at an atomic level further confirm the uniformly distributed Ni and uneven distribution Mo on the surface. This catalyst after OER was collectively denoted as Ni_{cluster}/MoO_x. These results indicated, after OER, uniformly distributed Ni in Ni_{SA}-O/Mo₂C undergoes transformation of the configuration and has been agglomerated into very small clusters by applied potential.

DFT simulations

In order to further explore the influence of various bonding forms on the electrocatalytic properties of HER and OER, we first analyzed the charge density difference and bader charge. Importantly, all adsorption energy calculations are obtained on the basis of Ni_{SA}-O/Mo₂C correction to zero. As shown in the inset of Fig. 6a and Fig. S32, there is a tendency of transferring electrons from Ni site to adsorbates, and we could see explicitly the number of valence electrons of Ni increased when formed Ni-C bond on Mo₂C facet (Fig. 6b) compared with formed Ni-O bond in Mo₂C facet. Therefore, Ni atoms directly embed the plane (101) of Mo₂C has strong adsorption of protons and hydroxyl, while the surface incorporated O of Mo₂C would adjust the number of valence electrons of Ni, then weakening the adsorption capacity. So, the adsorption energies of Ni_{SA}-O/Mo₂C for proton and hydroxyl are much lower than those of Ni_{SA}-Mo₂C, which markedly reduces the likelihood of blocking active sites, thus improving the electrocatalytic properties of HER (Fig. 6a). In addition, we found the energy level of the d-band center of Ni_{SA}-O/Mo₂C (-1.66 eV) is much lower than that of

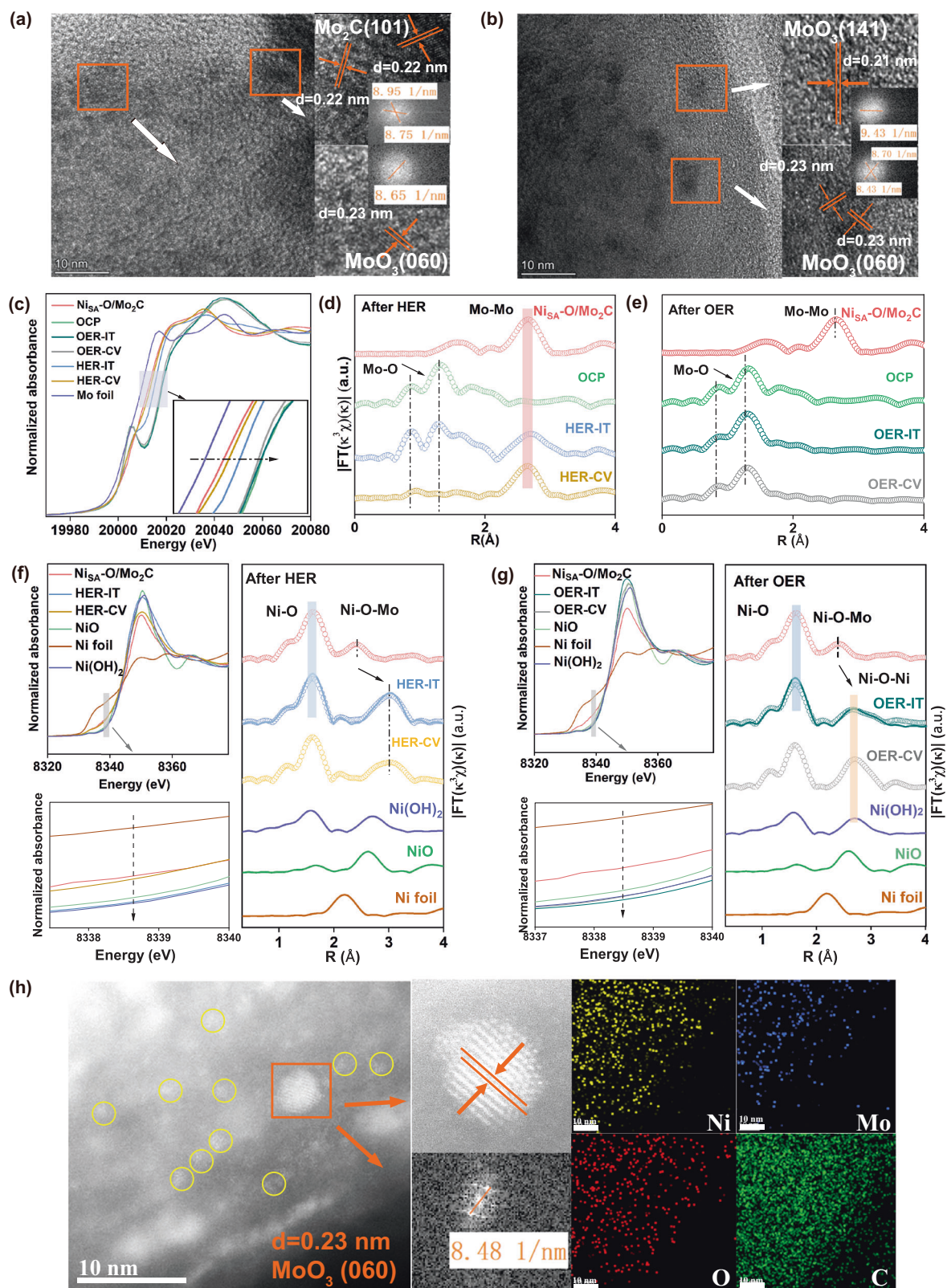


Fig. 5 | Structural analysis of the Ni_{SA}-O/Mo₂C after HER/OER to study active sites. **a, b** HRTEM images of Ni_{SA}-O/Mo₂C after HER/OER stability tests. **c–e** Ex situ Mo k-edge XANES and the corresponding FT-EXAFS curve of Ni_{SA}-O/Mo₂C, Ni_{SA}-O/Mo₂C-OCP, and Ni_{SA}-O/Mo₂C after HER/OER. **f–g** Ex situ XAS spectra

of Ni K-edge of Ni_{SA}-O/Mo₂C and the corresponding FT-EXAFS spectra after HER/OER, respectively. **h** HAADF-STEM image and EDS element mapping of Ni_{SA}-O/Mo₂C after OER.

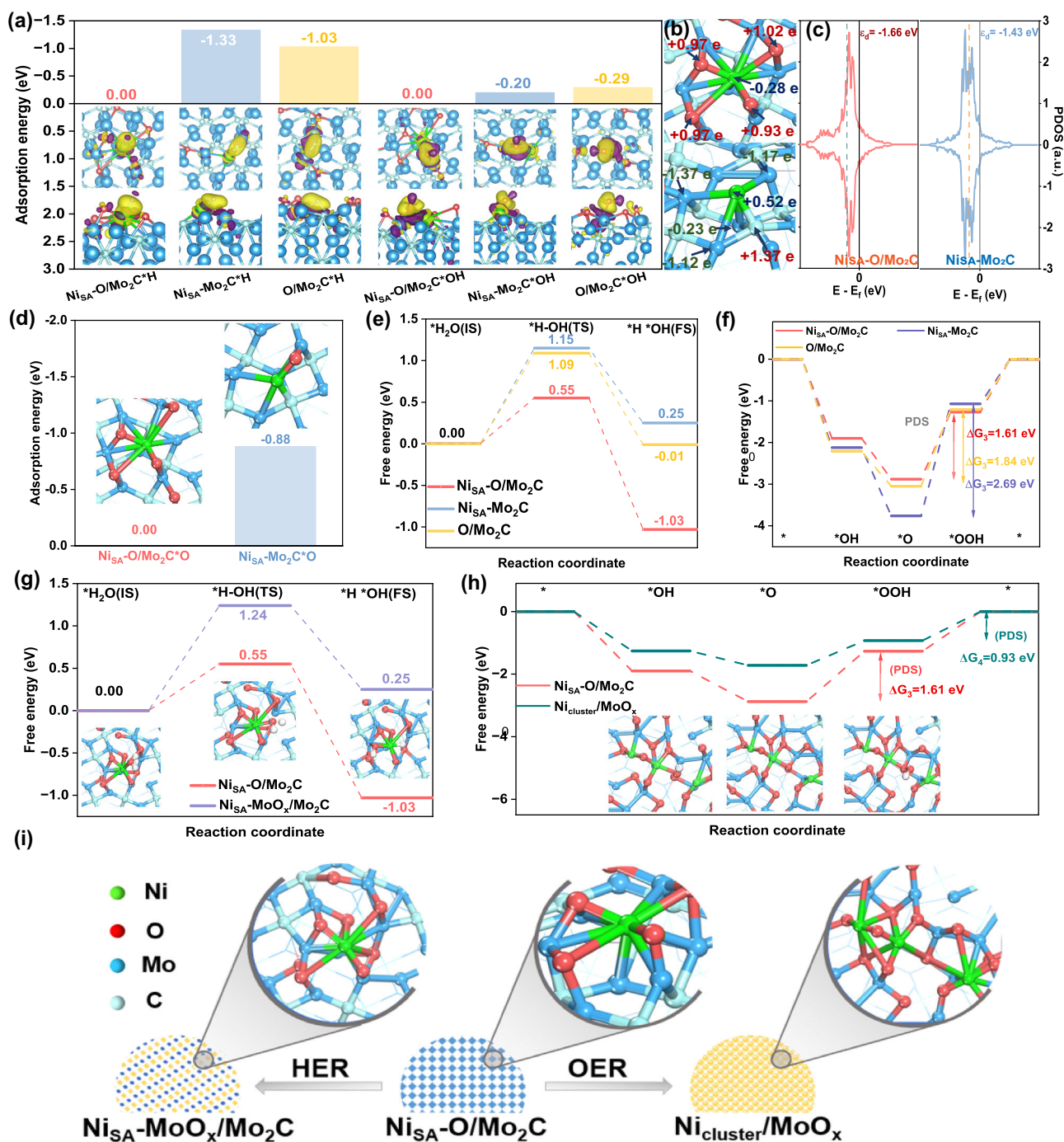


Fig. 6 | DFT calculation of HER and OER. **a** The chemisorption energies of *H and *OH in Ni sites of $Ni_{SA}\text{-O}/Mo_2C$, $Ni_{SA}\text{-}Mo_2C$ and O/Mo_2C . Insets are their 3D plots of charge density differences: top view and side view. **b** The number of bader charges transfer at specified Ni, O, and Mo atoms in $Ni_{SA}\text{-O}/Mo_2C$ and $Ni_{SA}\text{-}Mo_2C$. **c** PDOS graphs of $3d$ orbitals of Ni atoms in $Ni_{SA}\text{-O}/Mo_2C$ and $Ni_{SA}\text{-}Mo_2C$. The black dash lines show the d-band center (ϵ), and the Fermi level was taken as zero of energy.

d The chemisorption energies of O in Ni sites of $Ni_{SA}\text{-O}/Mo_2C$ and $Ni_{SA}\text{-}Mo_2C$. **e, g** Gibbs free energy diagram of Volmer step. Inset in **(g)**: the optimal models of different stage of $Ni_{SA}\text{-}MoO_x/Mo_2C$. **f, h** Gibbs free energy change of OER pathways on Ni sites. Inset in **(h)**: the atomic configurations of different stage of $Ni_{cluster}/MoO_x$. **i** Structural reconstitution of $Ni_{SA}\text{-O}/Mo_2C$ catalyst after different reaction process. Water blue = Mo, green = Ni, grey = C, red = O.

$Ni_{SA}\text{-}Mo_2C$ (-1.43 eV) (Fig. 6c). According to the d-band center theory, the lower electron density near of Fermi level will facilitate the desorption of adsorbate. So, compared with $Ni_{SA}\text{-O}/Mo_2C$, the $Ni_{SA}\text{-}Mo_2C$ had much stronger capacity of adsorbed O (Fig. 6d), which will lead to the higher overpotential of OER^{46,47}. We then calculated the potential barrier for hydrogen production and the energy barrier for Volmer step, as well as the overpotential of OER. As shown in Fig. S33 and Fig. 6e, the energy of the potential-determining step required by $Ni_{SA}\text{-O}/Mo_2C$ for hydrogen generation is 0.5 eV, much lower than those of

$Ni_{SA}\text{-}Mo_2C$ (0.65 eV) and O/Mo_2C (1.18 eV). In addition, the energy barrier of sluggish water dissociation for $Ni_{SA}\text{-O}/Mo_2C$ is 0.55 eV, which is lower than 1.15 eV of $Ni_{SA}\text{-}Mo_2C$ and 1.09 eV of O/Mo_2C , indicating Ni loaded on partially oxidized Mo_2C can improve HER performance. The processes of Volmer step are shown in Fig. S34. Meanwhile, the Potential Determining Step (PDS) for OER is the third electrochemical step from *O to *OOH , as we can see, $Ni_{SA}\text{-O}/Mo_2C$ remarkably decreases the energy barrier in this step to 1.61 eV, lower than that of O/Mo_2C (1.84 eV) and $Ni_{SA}\text{-}Mo_2C$ (2.69 eV) at $U=1.23$ V, indicating $Ni_{SA}\text{-}$

O/Mo₂C has much better performances, being consistent with the experimental observations. The diagram of OER reaction step was shown in Fig. S35.

Based on the above results, it would be found that the partially oxidized surface of Mo₂C facilitated the binding of Ni atoms via Ni-O and Ni-Mo (Ni-O-Mo) chemical bonds, thus promoting the electrocatalytic properties of HER and OER. However, the O/Mo₂C substrate of Ni_{SA}-O/Mo₂C after HER and OER underwent oxidation and dissolved. For Ni_{SA}-MoO_x/Mo₂C after HER (Fig. 6g, S36), we can see that its energy barrier of water dissociation is 1.24 eV, which becomes larger than that of Ni_{SA}-O/Mo₂C, indicating the overoxidation of the substrate can lead to some adverse hydrogen evolution effects. But for Ni_{cluster}/MoO_x after OER, the PDS changes from the step of *O to *OOH to the step of *OOH to O₂. Its free energy of the rate-determining step is 0.93 eV (Fig. 6h), which becomes smaller than that of Ni_{SA}-O/Mo₂C at U=1.23 V. In addition, compared with Ni_{SA}-O/Mo₂C, the reconstructed Ni_{cluster}/MoO_x shows a weaker adsorption capacity of O₂ (Fig. S37), indicating the reconstructed Ni_{cluster}/MoO_x accelerates the oxygen evolution reaction. These results indicate the overoxidation of the substrate is conducive to the aggregation of monatomic Ni into clusters and the improvement of oxygen evolution performance. Figure 6i shows the structural reconstitution of Ni_{SA}-O/Mo₂C catalyst after different reaction processes. These results are consistent well with the experimental observations.

In summary, we engineered a non-precious Ni single-atom bifunctional catalyst loaded on the surface of oxygen-incorporated Mo₂C via Ni-O-Mo bridge bonds (Ni_{SA}-O/Mo₂C). The obtained Ni_{SA}-O/Mo₂C catalyst exhibited an overpotential of 133 mV and 299 mV at the current density of 10 mA cm⁻² for HER and OER, respectively. Comprehensive characterizations and DFT calculations indicated that the surface oxygen atoms of Mo₂C were conducive to stabilizing the single atom Ni via the bridge bonding of Ni-O-Mo. The Ni-O-Mo bonding environment results in the regulation of electronic structures of single atom Ni towards an optimized proton and hydroxyl and moderate adsorption energy of O, which determines superior performance of the catalyst. Moreover, we found, that the configuration of atomically dispersed Ni in Ni_{SA}-O/Mo₂C electrocatalyst underwent transformation and O/Mo₂C support were oxidized and dissolved to varying degrees due to instability in KOH and the influence of applied potential. After HER, Ni species still maintain atomically dispersed form. However, after OER, the atomically dispersed Ni were agglomerated into very small clusters. In addition, we found overoxidized Mo₂C will lead to the configurations of single atom Ni to reconstruct, which will degrade its HER performance. However, compared with the original Ni_{SA}-O/Mo₂C, the potential-driven reconstituted small Ni clusters with optimal coordination structures are more favorable for OER. In a word, this work demonstrates a facile and feasible strategy to fabricate a low-cost and high-efficient bifunctional single-atom electrocatalyst and also provides guidance for further design of effective water-splitting electrocatalysts.

Methods

Synthesis of amorphous Mo-based precursor

The precursor Mo-based was first synthesized by a one-step hydrothermal method. Heat dissolved 1g of C₆H₁₂O₆ (1.00 g), 0.152 g of CH₄N₂S, and 0.132 g of C₁₀H₁₄MoO₆ in 50 mL of deionized water, when the solution changed from yellow-green to blue, it was transferred to a 100 mL Teflon-lined autoclave while hot. Then kept in an electric oven at the temperature of 200 °C for 48 h. After the autoclave was cooled down to room temperature, it was centrifuged three times with alternating water and ethanol, respectively. The sample was dried in a vacuum oven at 60 °C for 12 h.

Synthesis of Ni_{SA}-O/Mo₂C electrocatalysts

0.20 g of Mo-based precursor and 3 M (21.809 g) of Ni(NO₃)₂·6H₂O were dissolved in 10 mL of deionized water mixed with 15 mL of ethanol. Ultrasonically sonication dissolved for 40 min, constant temperature water bath at 40 °C for one night with continuous stirring. Then washed with ethanol for three times and dried to obtain the surface adsorbed Ni of Mo-based nanospheres. Finally, the sample was annealed at 300 °C for 1 h under an air atmosphere with a heating rate of 2 °C, to ensure that the C in the Mo-based nanospheres structure could escape with air, followed by 750 °C for 3 h under a hydrogen-argon atmosphere at the same rate of warming. The Ni_{SA}-O/Mo₂C was obtained after annealing.

Similarly, Ni_{1.4}-O/Mo₂C and Ni_{4.5}-O/Mo₂C was synthesized with the same method except for the doping amount of nickel nitrate (1.5 M and 4.5 M, respectively).

O/Mo₂C was synthesized by direct calcination of Mo-based precursors without Ni(NO₃)₂·6H₂O.

Structural characterization

The crystalline structure and phase purity were tested by X-ray diffraction pattern (XRD, Ultima, Japan) with Cu K α radiation at room temperature. The transmission electron microscopy (TEM) measurements were performed on Hitachi H-7650 operated at 2 kV. The Thermo Fisher IRIS Intrepid α system measured ICP-OES, which can be used to determine the element contents of the samples. High-resolution transmission electron microscopy (HR-TEM) and high-angle annular dark-field scanning transmission electron microscopy (HAADF-STEM) were carried out by Talos F200X G2 and JEOL JEM-2100F field emission electron microscope working at 200 kV, respectively. The X-ray photoelectron spectroscopy (XPS) experiments were tested on the PHI 5000 Versaprobe III spectrometer. The Brunauer-Emmett-Teller (BET) specific surface areas of typical products were performed at 77 K in a Belsorp-max surface area detecting instrument. N₂ adsorption-desorption experiments were carried out at 77 K on a Micromeritics ASAP 2460 Instrument. X-ray absorption spectroscopy (XAS) measurement and data analysis: X-ray absorption near-edge spectra (XANES) at the Mo K-edge obtained at 1W1B station in BSRF (Beijing Synchrotron Radiation Facility, P. R. China) operated at 2.5 GeV with a maximum current of 250 mA. The C-edge and N-edge were measured at beamline BL12B of the National Synchrotron Radiation Laboratory (NSRL) of China and the samples were deposited onto a double-sided carbon tap.

Electrochemical measurements

All spectra were collected in ambient conditions. Measurements of HER and OER activity of the electrocatalysts were performed with a traditional three-electrode system (CHI-760E), using a graphitic carbon rod as the counter electrode, Hg/HgO as the reference electrode, and a glassy carbon (GC) or carbon paper with the as-synthesized samples as the working electrode. 3.0 mg of sample and 20 μ L of 5 wt% Nafion solution were dispersed in 300 μ L of 1:1 v/v water/ethanol, then added 1.5 mg carbon black and sonicated for 30 min to form a homogeneous ink. Then 5 μ L of the solution was dispersed on a GC electrode of 3 mm diameter with a loading amount of 0.7 mg cm⁻². For the OER activity performed, 10.0 mg of sample and 50 μ L of 5 wt% Nafion solution in 1 mL of 1:1 v/v water/isopropanol, then 80 μ L of solution was dispersed on 1 \times 1 carbon paper with loading 0.74 mg cm⁻². All electrochemical OER and HER experiments were performed in a 1.0 M KOH solution, and polarization curves were iR-corrected. All potentials were referenced to the reversible hydrogen electrode (RHE), following the below equation:

$$E_{RHE} = E_{Hg/HgO} + 0.095 + 0.0591pH \quad (1)$$

The electrochemically active surface area (ECSA) of the as-synthesized samples without carbon black was estimated by the cyclic voltammetry (CV) measurements¹. The electrochemical double-layer capacitance was tested from 0.86 to 0.96 V (vs RHE) in 1M KOH solution for the HER or OER process at different scan rates (20, 40, 80, 100). The difference between the anode and cathode currents was plotted linearly against the scan rate, with the slope corresponding to the electrochemical double-layer capacitance (C_{dl}).

The ECSA was then estimated using the following equation:

$$ECSA = \frac{C_{dl}}{C_s} \quad (2)$$

Density Functional Theory Calculations

A series of density functional theory (DFT) calculations were all done with the Vienna Ab initio Simulation Package (VASP). The spin polarization was considered and calculated with Hubbard model. The electron-ion interaction was described using the projector augmented wave (PAW), and the kinetic energy cutoff for plane wave expansions was set to 450 eV. The electron exchange and correlation energies were treated within a generalized gradient approximation (GGA) in the Perdew-Burke-Ernzerhof (PBE) exchange-correlation. A DFT-D3 scheme of dispersion correction was used to describe the van der Waals (vdW) interactions in molecule adsorption. The Brillouin zone was sampled using the Monkhorst-Pack $2 \times 2 \times 1$ sampling and the convergence criteria were 1×10^{-6} eV in structure optimization, and force convergence criterion of -0.02 eV/Å. The electron smearing width of $\sigma = 0.05$ eV was employed according to the Methfessel-Paxton technique. To avoid the interactions between two adjacent periodic images, the vacuum thickness was set to be 15 Å, and to simulate the effect of inside a solid, we fixed two-layer atoms at the bottom.

The climbing image-nudged elastic band (CI-NEB) method was used to determine transition states (TS), with the energy convergence criteria of 1×10^{-7} eV and force convergence criteria of -0.03 eV/Å. The computed vibrational frequencies were used to characterize a minimum state without imaginary frequencies or an authentic transition state with only one imaginary frequency. The kinetic energy barrier (ΔG) of the Volmer step at alkaline HER is applied as an activity descriptor for catalytic performance, which can be calculated as follows:

$$\Delta G = G_{TS} - G_{IS} \quad (3)$$

where G_{TS} and G_{IS} are the free energy of the transition state and the initial state, respectively.

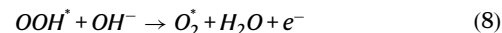
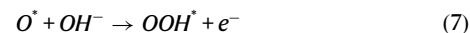
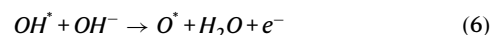
The free energy correction was obtained by including the zero-point energy (ZPE) and entropic contributions from vibrational degrees of freedom calculated with the substrate fixed, and the value gained by using Vaspkit.1.2.4.

The adsorption energy (E_{ad}) was calculated by subtracting the energies of the isolated adsorbate and the catalyst from the total energy of the adsorbed system:

$$E_{ad} = E_{slab+adsorbate} - E_{slab} - E_{adsorbate} \quad (4)$$

Where $E_{slab+adsorbate}$ is the total energy of adsorbate as adsorbed steadily at the active site. E_{slab} and $E_{adsorbate}$ are the total energy of the adsorbed surface and isolated adsorbate, respectively.

In alkaline media (pH = 14), the four-electron OER pathway may proceed through the following elementary steps:



Where the * refers to the catalytic, and the *one refers to the species that adsorbed on the activity sites.

Neglect PV contribution to translation for adsorbed molecules, the free energy of every step was calculated according to the equation of $G = E + H_{cor} - TS = E + G_{cor}$, where E is the energy of every species obtained from DFT calculations, and S are entropy, while T is 298.15 K. The H_{cor} and G_{cor} are the thermal corrections to enthalpy and the thermal correction to Gibbs free energy, respectively. These G_{cor} of *H, *O, *OH, and *OOH were taken from the frequency DFT calculation and got value by using Vaspkit.1.2.4.

The Gibbs free energy of the proton-electron pairs ($OH^- - e^- = H_2O - (H^+ + e^-)$) related in the PECT progress, whereas the fact that the proton-electron pairs is in equilibrium with gaseous H_2 at 0 V versus standard hydrogen electrode ($U = 0$, pH = 0, and pressure = 1 bar, and temperature = 298.15 K): $\mu(H^+ + e^-) = 1/2 \mu(H_2(g))$. According to Vaspkit.1.2.4, the internal energy of gas molecular gained from the formula: $U(T) = ZPE + \Delta U(O-T)$, the enthalpy of gas molecular gained from the formula: $H(T) = U(T) + PV = ZPE + \Delta U(O-T) + PV$, and the Gibbs free energy of gas molecular gained from the formula: $G(T) = H(T) - TS = ZPE + \Delta U(O-T) + PV - TS = E_{DFT} + G_{cor}$. Where E_{DFT} is the energy of the free gas molecule obtained from DFT calculations, G_{cor} is the thermal correction to Gibbs free energy of the free gas molecule obtained from the frequency DFT calculation and got value by using Vaspkit.1.2.4, with the temperature of 298.15 K, the pressure of H_2O and H_2 were 0.035 atm and 1 atm, respectively, and both H_2O and H_2 input 1 as the value of spin multiplicity. Note that the free energy of an O_2 gas molecule should be calculated by this equation: $G(O_2, g) = 2^*G(H_2O, g) - 2^*G(H_2, g) + 4.92$ eV.

The d-band center of the 3d orbitals of Ni sites obtained from their PDOS by using equation:

$$\varepsilon_d = \frac{\int_{-\infty}^{+\infty} \varepsilon f(\varepsilon) d\varepsilon}{\int_{-\infty}^{+\infty} f(\varepsilon) d\varepsilon} \quad (10)$$

where, the $f(\varepsilon)$ is the PDOS of an energy level of ε .

The charge density difference was evaluated using the formula $\Delta\rho = \rho(\text{substrate} + \text{adsorbate}) - \rho(\text{adsorbate}) - \rho(\text{substrate})$, then analyzed by using the VESTA code.

Construction of structure

Mo₂C. A 2x3 supercell surface consisting of 144 atoms from a cleaving surface of plane (1 0 1) of orthorhombic Mo₂C primitive cell was used firstly, and the fractional thickness set to 2.0, then adding 15 Å vacuum thickness to build vacuum slab crystal. The Brillouin zone integration is performed using the uniformly distributed scattering of going through the Gamma point to select a 2x2x1 k-mesh in the Monkhorst-Pack grid to make structure optimization, and we select 3x3x1 k-mesh to do density of state (DOS) calculations.

O/Mo₂C. A partially oxidized surface of Mo₂C is constructed by loading six oxygen atoms at the most stable adsorption site on the surface of Mo₂C.

Ni_{5A}-Mo₂C: A Ni atom coordinating with C atom is loaded in Mo₂C-O₆ surface.

Ni_{SA}-Mo₂C. The Mo₂C surface is loaded with more oxygen atoms to simulate a further oxidized surface, and then a nickel atom coordinating with four oxygen atoms is loaded on the surface.

Ni_{SA}-MoO_x/Mo₂C. The Mo₂C surface is loaded with more oxygen atoms to simulate a further oxidized surface and some of the carbon atoms are replaced by oxygen atoms to form a partially disordered MoO_x surface, then a nickel atom coordinating with six oxygen atoms is loaded on the surface.

Ni_{cluster}/MoO_x. The Mo₂C surface is loaded with more oxygen atoms to simulate a further oxidized surface and some of the carbon atoms are replaced by oxygen atoms to form a partially disordered MoO_x surface, then three nickel atoms coordinating with six oxygen atoms, respectively, are loaded on the surface.

To simulate the effect inside a solid, the atoms located in the lower half of the slab were fixed for all calculation models.

Data availability

The data that support the findings of this study are available from the corresponding author upon reasonable request.

References

- Wang, Q. et al. Ultrahigh-loading of ir single atoms on nio matrix to dramatically enhance oxygen evolution reaction. *J. Am. Chem. Soc.* **142**, 7425–7433 (2020).
- Chu, S. & Majumdar, A. Opportunities and challenges for a sustainable energy future. *Nature* **488**, 294–303 (2012).
- Roger, I., Shipman, M. A. & Symes, M. D. Earth-abundant catalysts for electrochemical and photoelectrochemical water splitting. *Nat. Rev. Chem.* **1**, 0003 (2017).
- Zhang, L. et al. Graphene defects trap atomic ni species for hydrogen and oxygen evolution reactions. *Chem* **4**, 285–297 (2018).
- Wang, H. et al. Bifunctional non-noble metal oxide nanoparticle electrocatalysts through lithium-induced conversion for overall water splitting. *Nat. Commun.*, **6**, 7261 (2015).
- Zhao, X. et al. Bifunctional electrocatalysts for overall water splitting from an iron/nickel-based bimetallic metal-organic framework/dicyandiamide composite. *Angew. Chem., Int. Ed.* **57**, 8921–8926 (2018).
- Shi, H., Liang, H., Ming, F. & Wang, Z. Efficient overall water-splitting electrocatalysis using lepidocrocite vooh hollow nanospheres. *Angew. Chem., Int. Ed.* **56**, 573–577 (2017).
- Luo, W. et al. A review: research progress of neural probes for brain research and brain-computer interface. *ACS Catal* **12**, 1167–1179 (2022).
- Yang, Y. et al. Hierarchical nanoassembly of mos(2)/co(9)s(8)/ni(3)s(2)/ni as a highly efficient electrocatalyst for overall water splitting in a wide ph range. *J. Am. Chem. Soc.* **141**, 10417–10430 (2019).
- Wang, M. et al. Interfacial water activation by single-atom co–n3sites coupled with encapsulated co nanocrystals for accelerating electrocatalytic hydrogen evolution. *ACS Catalysis* **12**, 10771–10780 (2022).
- Yin, J. et al. Iridium single atoms coupling with oxygen vacancies boosts oxygen evolution reaction in acid media. *J. Am. Chem. Soc.* **142**, 18378–18386 (2020).
- Jiang, K. et al. Dynamic active-site generation of atomic iridium stabilized on nanoporous metal phosphides for water oxidation. *Nat. Commun.* **11**, 2701 (2020).
- Wang, W. et al. Confining zero-valent platinum single atoms in α -moc1-xfor ph-universal hydrogen evolution reaction. *Adv. Funct. Mater.* **32**, 2108464 (2021).
- Kuang, M., Han, P., Wang, Q., Li, J. & Zheng, G. CuCo hybrid oxides as bifunctional electrocatalyst for efficient water splitting. *Adv. Funct. Mater.* **26**, 8555–8561 (2016).
- Zhu, Y. et al. A perovskite nanorod as bifunctional electrocatalyst for overall water splitting. *Adv. Energy Mater.* **7**, 1602122 (2017).
- Li, M. et al. Proximity electronic effect of ni/co diatomic sites for synergistic promotion of electrocatalytic oxygen reduction and hydrogen evolution. *Adv. Funct. Mater.* **33**, 2210867 (2022).
- Yang, H., Wu, Y., Zhuang, Z., Li, Y. & Chen, C. Computational probing of temperature-dependent unfolding of a small globular protein: from cold to heat denaturation. *Chin. J. Chem.* **40**, 515–523 (2021).
- Yuan, S. et al. Dual synergistic effects between Co and Mo2C in Co/Mo2C heterostructure for electrocatalytic overall water splitting. *Chem. Eng. J.* **430**, 132697 (2022).
- Yu, Y., Zhou, J. & Sun, Z. Novel 2D transition-metal carbides: ultra-high performance electrocatalysts for overall water splitting and oxygen reduction. *Adv. Funct. Mater.* **30**, 2000570 (2020).
- Anjum, M. A. R., Lee, M. H. & Lee, J. S. Boron- and nitrogen-codoped molybdenum carbide nanoparticles imbedded in a bcn network as a bifunctional electrocatalyst for hydrogen and oxygen evolution reactions. *ACS Catal* **8**, 8296–8305 (2018).
- Das, D., Santra, S. & Nanda, K. K. In situ fabrication of a nickel/molybdenum carbide-anchored n-doped graphene/cnt hybrid: an efficient (Pre)catalyst for OER and HER. *ACS Appl. Mater. Interfaces* **10**, 35025–35038 (2018).
- Li, M. et al. Ni strongly coupled with mo2c encapsulated in nitrogen-doped carbon nanofibers as robust bifunctional catalyst for overall water splitting. *Adv. Energy Mater.* **9**, 1803185 (2019).
- Xiao, M. et al. Molten-salt-mediated synthesis of an atomic nickel co-catalyst on tio2for improved photocatalytic h2evolution. *Angew. Chem., Int. Ed.* **59**, 7230–7234 (2020).
- Suryanto, B. H. R., Wang, Y., Hocking, R. K., Adamson, W. & Zhao, C. Overall electrochemical splitting of water at the heterogeneous interface of nickel and iron oxide. *Nat. Commun.* **10**, 5599 (2019).
- Hu, F. et al. Lattice-Matching formed mesoporous transition metal oxide heterostructures advance water splitting by active Fe–O–Cu bridges. *Adv. Energy Mater.* **12**, 2000067 (2022).
- Tang, C. et al. Electronic Coupling of Single Atom and FePS₃ Boosts Water Electrolysis. *Energy Environ. Sci.* **5**, 899–905 (2022).
- Li, G. et al. The synergistic effect of Hf–O–Ru bonds and oxygen vacancies in Ru/HfO(2) for enhanced hydrogen evolution. *Nat. Commun.* **13**, 1270 (2022).
- Li, R. et al. Potential-dependent reconstruction of Ni-based cuboid arrays for highly efficient hydrogen evolution coupled with electro-oxidation of organic compound. *Chem. Eng. J.* **453**, 139797 (2023).
- Zhao, Y. et al. Dynamics and control of active sites in hierarchically nanostructured cobalt phosphide/chalcogenide-based electrocatalysts for water splitting. *Energy Environ. Sci.* **15**, 727–739 (2022).
- Zhou, H. et al. Electrocatalytic upcycling of polyethylene terephthalate to commodity chemicals and H(2) fuel. *Nat. Commun.* **12**, 4679 (2021).
- Li, S. et al. Oxygen-evolving catalytic atoms on metal carbides. *Nat. Mater.* **20**, 1240–1247 (2021).
- Zhang, P. et al. Bifunctional single atom catalysts for rechargeable zinc–air batteries: from dynamic mechanism to rational design. *Adv. Mater.* **35**, 2303243 (2023).
- Zhou, L., Zhao, D. & Lou, X. W. Double-shelled CoMn2O4 hollow microcubes as high-capacity anodes for lithium-ion batteries. *Adv. Mater.* **24**, 745–748 (2012).
- Guan, J., Mou, F., Sun, Z. & Shi, W. Preparation of hollow spheres with controllable interior structures by heterogeneous contraction. *Chem. Commun.* **46**, 6605–6607 (2010).
- Han, L. et al. Atomically dispersed molybdenum catalysts for efficient ambient nitrogen fixation. *Angew. Chem., Int. Ed.* **58**, 2321–2325 (2019).
- Wang, Q. et al. Single iridium atom doped ni(2)p catalyst for optimal oxygen evolution. *J. Am. Chem. Soc.* **143**, 13605–13615 (2021).

37. Wei, H. et al. Molybdenum carbide nanoparticles coated into the graphene wrapping n-doped porous carbon microspheres for highly efficient electrocatalytic hydrogen evolution both in acidic and alkaline media. *Adv. Sci.* **5**, 1700733 (2018).
38. Yu, L., Yang, J. F., Guan, B. Y., Lu, Y. & Lou, X. W. D. Hierarchical hollow nanoprisms based on ultrathin ni-fe layered double hydroxide nanosheets with enhanced electrocatalytic activity towards oxygen evolution. *Angew. Chem., Int. Ed.* **57**, 172–176 (2018).
39. Han, W. et al. Ultra-small Mo₂C nanodots encapsulated in nitrogen-doped porous carbon for pH-universal hydrogen evolution: insights into the synergistic enhancement of HER activity by nitrogen doping and structural defects. *J. Mater. Chem. A* **7**, 4734–4743 (2019).
40. Jin, H. et al. In situ cobalt-cobalt oxide/N-doped carbon hybrids as superior bifunctional electrocatalysts for hydrogen and oxygen evolution. *J. Am. Chem. Soc.* **137**, 2688–2694 (2015).
41. Zhuang, Z. et al. Atomically dispersed nonmagnetic electron traps improve oxygen reduction activity of perovskite oxides. *Energy Environ. Sci.* **14**, 1016–1028 (2021).
42. Qin, J. et al. Activating edge-Mo of 2H-MoS₂ via coordination with pyridinic N-C for pH-universal hydrogen evolution electrocatalysis. *ACS Catal.* **11**, 4486–4497 (2021).
43. Chen, W.-F. et al. Reply to comments on "synthesis, characterization, and structures of persistent aniline radical cation". *Energy Environ. Sci.* **6**, 943–945 (2013).
44. Aracena, A., Sanino, A. & Jerez, O. Dissolution kinetics of molybdenite in KOH media at different temperatures. *T NONFERR METAL SOC* **28**, 177–185 (2018).
45. He, Z. et al. Activating lattice oxygen in NiFe-based (oxy)hydroxide for water electrolysis. *Nat. Commun.* **13**, 2191 (2022).
46. Nørskov, J. K. et al. Origin of the overpotential for oxygen reduction at a fuel-cell cathode. *J. Phys. Chem. B* **108**, 17886–17892 (2004).
47. Nørskov, J. K., Abild-Pedersen, F., Studt, F. & Bligaard, T. Density functional theory in surface chemistry and catalysis. *Proc. Natl Acad Sci USA.* **108**, 937–943 (2011).

Acknowledgements

This work was supported by the National Key R&D Program of China (2023YFB4005100), National Natural Science Foundation of China (22309011, 52272186, 22105116, 21872008, 52173232, 21925202, U22B2071), Yunnan Provincial Science and Technology Project at Southwest United Graduate School (202302AO370017), International Joint Mission On Climate Change and Carbon Neutrality, Beijing Institute of Technology Research Fund Program for Young Scholars. We thank the 1W1B station for XAFS measurements in the Beijing Synchrotron Radiation Facility (BSRF) and Dr. Fang Zhang from Analysis & Testing center, Beijing Institute of Technology.

Author contributions

D.Z., J.T.Z., M.H.C., and C.C. supervised the project. M.Y.H. and D.Z. designed the work and carried out most of the experiments. L. R. Z. guided the XANES, ex situ XAS measurements, and analyzed XAS results. W.Y.F., X.T., J.T. F.T. X.W. helped to prepare samples and character the samples with TEM and XPS. All the authors discussed the results and assisted during the manuscript preparation.

Competing interests

The authors declare no competing interests.

Additional information

Supplementary information The online version contains supplementary material available at <https://doi.org/10.1038/s41467-024-45533-3>.

Correspondence and requests for materials should be addressed to Di Zhao, Minhua Cao, Jiatao Zhang or Chen Chen.

Peer review information *Nature Communications* thanks Uday Maiti and the other, anonymous, reviewer(s) for their contribution to the peer review of this work. A peer review file is available.

Reprints and permissions information is available at <http://www.nature.com/reprints>

Publisher's note Springer Nature remains neutral with regard to jurisdictional claims in published maps and institutional affiliations.

Open Access This article is licensed under a Creative Commons Attribution 4.0 International License, which permits use, sharing, adaptation, distribution and reproduction in any medium or format, as long as you give appropriate credit to the original author(s) and the source, provide a link to the Creative Commons license, and indicate if changes were made. The images or other third party material in this article are included in the article's Creative Commons license, unless indicated otherwise in a credit line to the material. If material is not included in the article's Creative Commons license and your intended use is not permitted by statutory regulation or exceeds the permitted use, you will need to obtain permission directly from the copyright holder. To view a copy of this license, visit <http://creativecommons.org/licenses/by/4.0/>.

© The Author(s) 2024